Nano Research

Open Access

Research Article

Amide-modulated crystallization kinetics for high-performance pure-blue perovskite LED

Zhiying Guo[1], Ruoyan Liu[1], Bei Zhou[1], Mohan Li[1], Zhijun Liu[1], Lanlan Zhai[1], Qian Miao[1], He Huang[1], Yun Yang[1], Guoku Chao[1] ✉, Haihong Wen[2], Jun Zou[3,4] ✉, and Chao Zou[1] ✉

[1] *College of Chemistry and Materials Engineering, Wenzhou University, Wenzhou 325027, China*
[2] *National and Local Joint Engineering Research Centre of Ecological Treatment Technology for Urban Water Pollution, Wenzhou University, Wenzhou 325035, China*
[3] *Institute of New Materials & Industrial Technology, Wenzhou University, Wenzhou 325024, China*
[4] *School of Science, Shanghai Institute of Technology, Shanghai 201418, China*

Cite this article: *Nano Research*, **2026**, *19*, 94907920. https://doi.org/10.26599/NR.2025.94907920

ABSTRACT: Quasi-two-dimensional perovskites, with spectral tuning property, have opened up vast application prospects in the field of optoelectronic devices, especially in blue perovskite light-emitting diode (PeLED). However, relatively high density of defect states usually results in nonradiative recombination loss due to unexpected carriers capture at prolonged transport, which limits high-performance PeLED. Here, we propose a method for preparing pure-blue PeLED using bifunctional amide molecules to modulate crystallization kinetics. This strategy inhibits the formation of the *n* = 1 phase and simultaneously passivates defects with the bifunctional groups, thereby reducing the occurrence of nonradiative recombination. The external quantum efficiency of the pure-blue PeLED fabricated using this strategy is significantly enhanced, reaching 9.7% at 478 nm, which is about 7 times higher than that of the control device. This work provides a novel strategy on the selection of bifunctional passivators for perovskites.

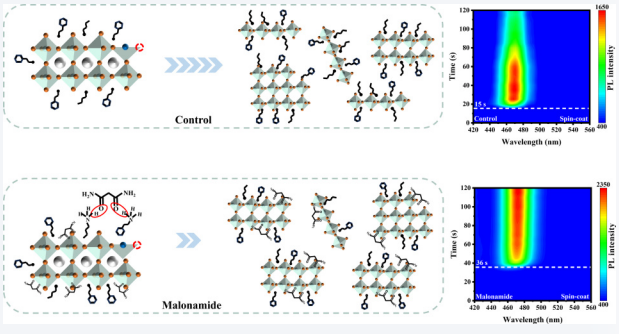

KEYWORDS: quasi-two-dimensional (2D), perovskite, pure-blue, perovskite light-emitting diode (PeLED), crystallization kinetics

1 Introduction

In recent years, perovskite light-emitting diode (PeLED) has been regarded as promising candidates for the next generation of lighting technology due to their advantages such as high color purity, low cost, and tunable emission spectrum characteristics [1–5]. Since the first demonstration of perovskite in 2009 for solar cell and in 2014 for LED, the performance of blue, green, red, and near-infrared PeLED has been improved rapidly, with external quantum efficiency (EQE) exceeding 25% [6–11]. Despite the achievement of blue light emission, the efficiency of blue PeLED remains relatively low, especially under operational condition [12]. The fabrication of efficient and stable blue PeLED remains a challenge, impeding their commercialization in full-color display applications. As previously reported, blue light emission from perovskites can be achieved through two primary methods. One approach involves using composition engineering to construct mixed Br/Cl systems to adjust the bandgap, enabling a transition from green to blue emission by increasing the chloride ion content in the thin film [13–15]. Another method introduces organic spacer cations to control the dimension of perovskites, producing a quantum confinement effect that blue-shifts the emission spectrum [16–18]. For efficient blue PeLEDs, quasi-two-dimensional (quasi-2D) perovskites with mixed Br/Cl have emerged, taking advantages of their broadened bandgap and higher exciton-binding energies to achieve excitons refined [19–21].

In fact, two factors are responsible for the compromised EQE of blue PeLED within quasi-2D perovskite emission layer. To elaborate, the first contributing element stems from the characteristics of blue perovskite themselves. Their comparatively broad bandgap, coupled with inherent structural instability, triggers

Received: June 23, 2025; **Revised:** August 7, 2025
Accepted: August 13, 2025

✉Address correspondence to Guoku Chao, 00112001@wzu.edu.cn; Jun Zou, zoujun@sit.edu.cn; Chao Zou, zouchao@wzu.edu.cn

electric-field-driven halide ion migration and phase separation phenomenon. Under excitation conditions, halide ions exhibit a propensity to migrate toward adjacent vacancies, inducing spectral instability and spectral shifts that subsequently lead to degradation in device efficiency [19, 20]. The second pivotal factor relates to the crystallographic imperfections in quasi-2D perovskite structures. The defect states originating from lattice distortion-induced bandgap widening act as charge carrier traps during energy transfer processes, thereby constraining the available carrier population and suppressing radiative emission efficiency [21, 22]. Furthermore, quasi-2D perovskites with multiphase compositions exhibit abundant microcrystalline boundaries and heterointerfaces, which are prone to generate defect sites facilitating non-radiative recombination. Consequently, precise control of phase alignment and effective mitigation of intrinsic defects in quasi-2D perovskite systems are critical for achieving high-performance blue PeLED with superior luminous efficacy.

Currently, defect passivation has proven to be an effective strategy for enhancing the photoelectric performance of perovskites, which can be implemented by adding additives to the perovskite precursor solution [23, 24]. Long-chain organic ammonium with better thermal stability is used to replace volatile methylammonium (MA^+, $CH_3NH_3^+$) or formamidinium (FA^+, $HC(NH_2)_2^+$) to suppress the formation of organic ammonium vacancies, thereby passivating halide defects [25]. Small molecules with functional groups (C=O, P=O S=O, $-NH_2$) [26–29] were also introduced into perovskite layer, as these functional groups can form strong bonds with Pb to reduce the density of Pb defects. Indeed, the defects persistence of halide and uncoordinated lead ions within quasi-2D perovskite, derived from intrinsic soft crystal lattice feature and unexpected n = 1 phase, which owns more trap state and strong exciton–phonon coupling, result in nonradiative recombination losses [30, 31]. Actually, both organic ammonium and small molecules play roles in modulating crystallization kinetics and suppressing defects formation, which determines quality of desired perovskite, specifically, lessening the deviation from expected ion orders in quasi-2D perovskite. One can expect that modulating the crystallization process will produce high-quality perovskite, since controlled crystal growth exhibits ordered lattice arrangement than nonintervention. The additives with multifunctional groups will provide such opportunity, owing to their multi-roles endowed by functional groups. Currently, strategies for modulating crystallization process by multifunctional groups, which suppresses unexpected n = 1 phase and the formation of defects, are the promising focus, enabling high-performance PeLED.

In this work, we introduced amide additives to manipulate crystallization kinetics and thus the distribution of n-phases in perovskites. Specifically, upon the incorporation of medium-chain-length malonamide as an additive, crystallization kinetics of quasi-2D perovskite was regulated by the double-hydrogen bond between perovskite layers, and the n = 1 phase was markedly suppressed, thereby reducing the occurrence of nonradiative recombination. We observed that the C=O groups in malonamide formed C=O···Pb interactions with the uncoordinated Pb ions in perovskites at suitable angles, while the double $-NH_2$ groups formed N–H···Br^-/Cl^- hydrogen bonds. These interactions collectively contributed to manipulating small-n phases and passivating defects. The medium-chain-length amide additive, malonamide, demonstrated notable advantages in this context, and these synergistic effects allow to achieve high-performance pure-blue PeLED with EQE increasing from 1.4% at 473 nm to 9.7% at 478 nm.

2 Experimental

2.1 Materials

Poly(3,4-ethylenedioxythiophene):poly(styrenesulfonate) (PEDOT:PSS, AI 4083), phenethylamine bromide (PEABr, 99.5%), butylamine bromide (BABr, 99.5%), formamidinium bromide (FABr, 99.9%), cesium chloride (CsCl, 99.9%), lead bromide ($PbBr_2$, 99.9%), and 2,2',2"-(1,3,5-benzinetriyl)-tris(1-phenyl-1-H-benzimidazole) (TPBi, 99.9%) were purchased from Xi'an Yuri Solar Co., Ltd. Dimethyl sulfoxide (DMSO, 99.9%) was purchased from Aladdin. LiF (99.98%) was purchased from Sigma-Aldrich. Oxamide, malonamide, and succinamide were purchased from Meryer Biochemical Technology Co., Ltd., and aluminum was purchased from ZhongNuo Advanced Material Technology Co. Ltd. All the materials were used as received without any purification.

2.2 Preparation of perovskite precursor

The perovskite precursor solution was prepared by dissolving PEABr, BABr, CsCl, FABr, and $PbBr_2$ in 1 mL DMSO in the N_2-filled glovebox. Perovskite solutions were prepared using a concentration of 0.20 M based on $PbBr_2$, and the molar ratio was 0.6:0.4:1.1:0.075:1.0 for PEABr:BABr:CsCl:FABr:$PbBr_2$. After stirring for 4 h at 30 °C, amides were added into the perovskite precursor separately, then stirring for 2 h. All precursor solutions were filtered through 0.22 μm filter before use.

2.3 Device fabrication

The indium tin oxide (ITO) substrates were ultrasonically cleaned in deionized water with detergent, ethanol, acetone, iso-propanol, and ethanol solution for 20 min. Prior to the spin-coating of the PEDOT:PSS, the cleaned ITO substrates were treated with ultraviolet O_3 for 15 min. The PEDOT:PSS was spin-coated onto the ITO substrates at 4000 rpm for 40 s, followed by annealing on a hot plate at 150 °C for 20 min in air. Then, the PEDOT:PSS films were modified by spin-coating the LiF aqueous solutions (2.0 mg·mL^{-1}) at 5000 rpm for 40 s followed by annealing at 150 °C for 20 min in air [32, 33]. The precursor solution was spin-coated at 4000 rpm for 120 s and annealed at 80 °C for 5 min in glovebox. Finally, TPBi (50 nm), LiF (1 nm), and Al (113 nm) were successively thermal evaporated onto the substrate in the vacuum evaporator chamber under a pressure of 5×10^{-4} Pa. The active area of each separating device was 8 mm^2, and it was tested in atmospheric environments after encapsulation by epoxy resins.

2.4 Characterizations

Ultraviolet–visible (UV–vis) absorption spectra were measured by using a SHIMADZU UV-1800. Grazing incidence X-ray diffraction (GIXRD) patterns of the prepared samples were recorded with Bruker D8 advance X-ray diffractometer with graphite monochromatized Cu Kα (λ = 1.5405 Å) radiation. The steady-state photoluminescence (PL) and time-resolved PL (TRPL) spectra, and photoluminescence quantum yield (PLQY) were obtained by an FLS980 spectrofluorometer (Edinburgh Instruments, Ltd.). The excitation source was 365 nm from a Xe lamp for PL, and the time-resolved luminescence decay was measured using time-correlated

single photon counting with a 375 nm laser. X-ray photoelectron spectroscopy (XPS) was performed by Thermo Fisher ESCALAB 250Xi, and the curves were corrected based on the C 1s peak at 284.8 eV. ^{1}H nuclear magnetic resonance (NMR) measurements were performed with a Quantum-I-Plus 400 NMR spectrometer (FT, 400 MHz for ^{1}H) using deuterated DMSO-*d*6 as the solvent. The Fourier transform infrared spectroscopy (FTIR) spectra were recorded with a Thermo Fisher iS50 FTIR. For the FTIR samples, powder mixed with perovskite solution was prepared before drying. space-charge-limited current (SCLC) measurements were conducted using hole-only devices, and the resultant curves were fitted with the Mott–Gurney law given by $J = 9\varepsilon_0\varepsilon\mu V^2/8L^3$, where J is the current density. The current density–voltage–luminance (J–V–L) characteristics and EQE–J curves of the device were tested by spectrometers equipped with Keithley 2400 fiber integrating spheres and an Ocean Optics QE65 Pro spectrometer. The transient absorption spectroscopy (TAS) was performed with a femtosecond transient absorption spectrometer (TA-100) using 350 nm pump pulses as the excitation wavelength.

2.5 Computational methods

The quantum chemistry calculations were carried out with the ORCA 5.0.4 [34] software. The RIJCOSX technique [35] was enabled to significantly accelerate the calculation. The B3LYP [36] functional and the basis set of def2-SVP [37] were adopted for the geometry optimization and frequency calculations in combination with the density functional theory (DFT)-D4 [38, 39] dispersion correction. The geometries were fully optimized without any structural constraints. The frequency calculations were carried out at the same level of theory to verify that all structures have no imaginary frequency. The single point energy was calculated at the B3LYP-D4/ma-def2-TZVP [37, 40] level of theory. The electrostatic potential (ESP) and input files of ORCA program were prepared with the help of Multiwfn [41–43] code. The geometric structure figures and ESP figures were rendered by means of the VMD [44] visualization program.

3 Result and discussion

3.1 Manipulation on crystallization kinetics

The precursor solution was prepared by dissolving CsCl, PEABr, BABr, FABr, and $PbBr_2$ into DMSO with precisely controlled molar ratio to form quasi-2D perovskite films for blue emission. To investigate the crystallization kinetics of quasi-2D perovskite films, we conducted *in-situ* PL measurements during the spin-coating process. During spin-coating, following the evaporation of the DMSO solvent, quasi-2D perovskite continuously crystallizes from a precursor solution dominated by ionic interactions between metal cations and halide anions [45]. In the control, the perovskite emitters form at approximately 15 s from the initiation of the spin-coating process, subsequently exhibiting a strong PL signal attributed to the rapid growth of perovskite crystals (Fig. 1(a)). After about 70 s, this signal displays a slow and continuous decline, indicating PL quenching. This quenching phenomenon can be ascribed to the rapid crystallization of perovskite emitters, during which irregular arrangement of nanoparticles leads to the formation of numerous defect-rich regions [46, 47]. By incorporating malonamide additive, the perovskite exhibits a detectable fluorescent signal only after 36 s of spin-coating (Figs. 1(b) and 1(c)). The fluorescent signal gradually increases during the whole spin-coating process and the continuous PL drop completely disappears, suggesting that the addition of malonamide induces delayed crystallization in the perovskite film and effectively suppresses the luminescence quenching phenomenon [48]. In addition to malonamide, the inclusion of oxamide or succinamide displays the similar trend on the PL evolution (Fig. S1 in the Electronic Supplementary Material (ESM)). Sequential annealing process for perovskite films exhibits red shift peak of PL at all samples (Fig. S2 in the ESM), which results from the grains growth in the coarsening process.

To reveal why the amide-treated perovskites have distinct crystallization process, we performed DFT calculations to show the ESP for understanding the electronic structures of three amide molecules, as depicted in Fig. 2(a). The C=O and $-NH_2$ groups exhibit obviously negative (blue region) and positive (red region) potential, respectively, suggesting that the amide can serve as a Lewis acid and base [49]. Nucleophilic C=O possesses electronegativity, enabling it to serve as a Lewis base for passivating uncoordinated Pb ions through Lewis acid-base interactions. Besides, nucleophilic C=O possesses the possibility to form hydrogen bonds with ammonium group of PEA^+/BA^+. Conversely, the electrophilic $-NH_2$ group exhibits electropositivity, functioning as Lewis acid forming hydrogen bonds with $Pb(Br/Cl)_6^{4-}$ octahedra in perovskite crystals [50]. FTIR was utilized to investigate the interaction between malonamide and perovskite. The FTIR spectra of malonamide and the mixture of malonamide and perovskite are depicted in Fig. 2(b). The peaks located at 1694, 1668, 1632 cm^{-1} can be identified as the C=O, and the peaks at 3389 and 3160 cm^{-1} are two characteristic peaks of $-NH_2$ in malonamide. After being added into perovskite, the peaks attributed to C=O group shift from 1694, 1668 to 1664 cm^{-1}, and enhanced intensity at 1632 cm^{-1} indicating

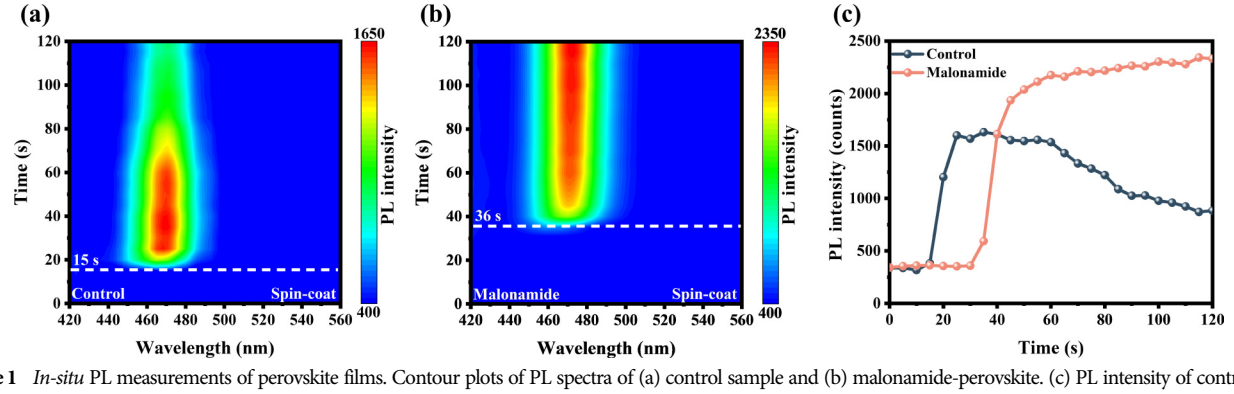

Figure 1 *In-situ* PL measurements of perovskite films. Contour plots of PL spectra of (a) control sample and (b) malonamide-perovskite. (c) PL intensity of control and malonamide-perovskite films.

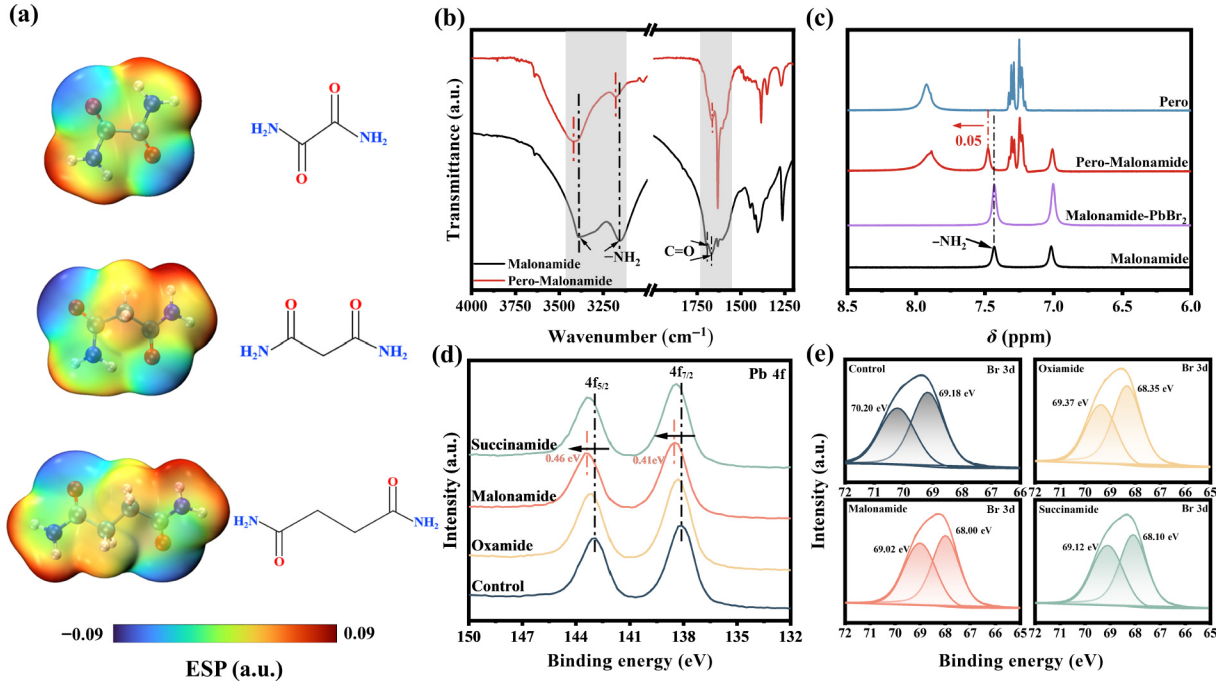

Figure 2 (a) Chemical structure and ESP of oxamide, malonamide, and succinamide. (b) FTIR curves of pure malonamide and malonamide-treated perovskite film. (c) ^{1}H NMR spectra of malonamide, the mixture with $PbBr_2$, and perovskite precursor. XPS spectra of (d) Pb 4f and (e) Br 3d of perovskite film.

that C=O of malonamide interacts with uncoordinated Pb^{2+} in perovskite. Additionally, the stretching vibration peaks of $-NH_2$ shift from 3389 and 3160 to 3416 and 3182 cm^{-1}, respectively, implying the N–H···Br^-/Cl^- hydrogen bonds were formed. The interaction between malonamide and perovskite was further confirmed by analyzing mixtures of malonamide using liquid NMR spectroscopy. As depicted in Fig. 2(c), the chemical shift at 7.43 ppm corresponds to the $-NH_2$ in malonamide. After introduced into perovskite, the chemical shift of $-NH_2$ in malonamide moves to 7.48 ppm due to the deshielding effect resulting from their interactions between nucleophilic C=O ammonium group in perovskite, confirmed by the same shift trends with PEABr/BABr (Fig. S3 in the ESM) and FABr (Fig. S4 in the ESM). Further, the broadened peaks at 7.88/7.72 ppm, attributed to $-NH_3^+$ of PEA^+/BA^+, verified the formation of hydrogen bonds. It is worth noting that the hydrogen bonding is enhanced by the interactions of N–H···Br^-/Cl^- when the perovskites begin to nucleate and crystallize as solid state, since abundant $Pb(Br/Cl)_6^{4-}$ octahedra appears in perovskite crystal with the solution consumed [51, 52].

To gain a deeper understanding of the roles of amides in perovskite, the XPS was conducted. The Pb $4f_{5/2}$ and Pb $4f_{7/2}$ binding energy peaks of control film were located at 142.96 and 138.11 eV, respectively (Fig. 2(d)). Upon amide treatment, these peaks experienced an upshift to higher binding energy; specifically, for malonamide-modified sample, the binding energies had an upshift of 0.46 eV for Pb $4f_{5/2}$ and 0.41 eV for Pb $4f_{7/2}$. The increase in binding energy indicates that the C=O functional group in malonamide and the uncoordinated Pb^{2+} in the perovskite are coordinated, thus diminishing the defects. The specific value of Br 3d binding energy change after different amide modification is summarized in Table S1 in the ESM. Clearly, the peaks of Br 3d all moved towards lower binding energy (Fig. 2(e)). It is worth noting that the most obvious shift of Br 3d peak was observed in malonamide-treated film, indicating the most powerful interaction with bromine. Accordingly, we speculate that more hydrogen bonds, N–H···Br^-/Cl^-, formed between $-NH_2$ on the two sides of malonamide and perovskite than other amides. The XPS results are consistent with the findings from FTIR and NMR spectra.

3.2 Phase distribution of perovskite

To probe the influences of additives on phase distribution of perovskite, we performed structural and optoelectronic characterization of films. GIXRD patterns indicate that alterations in the crystal structure of perovskite occur upon the introduction of malonamide additive (Figs. 3(a) and 3(b)). All quasi-2D perovskites display dominated (002) crystal planes at 3.8° for n = 2 phases, except for malonamide-treated perovskite, which shows shifts towards high angles. According to the Bragg's diffraction equation of $d = m\lambda/(2\sin\theta)$, n = 2 phases of malonamide-treated and malonamide-free perovskites have 21.4 and 24.2 Å interlayer distance, respectively. The reduced interplanar spacing d implies tighter layer-to-layer interactions in 2D perovskite, which are achieved by double-hydrogen bonds between hydrogen atoms of each terminal $-NH_2$ in malonamide and halogen atoms in octahedra $Pb(Br/Cl)_6^{4-}$. A schematic diagram illustrates the interaction of n = 2 phase of 2D perovskite constructed from PEA^+/BA^+ and malonamide (Fig. S5 in the ESM). When malonamide molecule combined with perovskite, double-hydrogen bonds between $-NH_2$ in two sides of malonamide and octahedra $Pb(Br/Cl)_6^{4-}$ in perovskite effectively reduce the van der Waals gap and enhance the interaction within perovskite layers, beneficial to the energy transfer efficiency [53]. Furthermore, the perovskite film with the addition of malonamide exhibits significantly enhanced diffraction peaks, indicating an improvement in the crystallinity upon the incorporation of the additive.

As shown in Fig. 3(c), three absorption peaks at 387, 414, and 440 nm appear in the perovskite film, corresponding to n = 1, 2, and 3 phases in the quasi-2D perovskites, respectively. Upon the

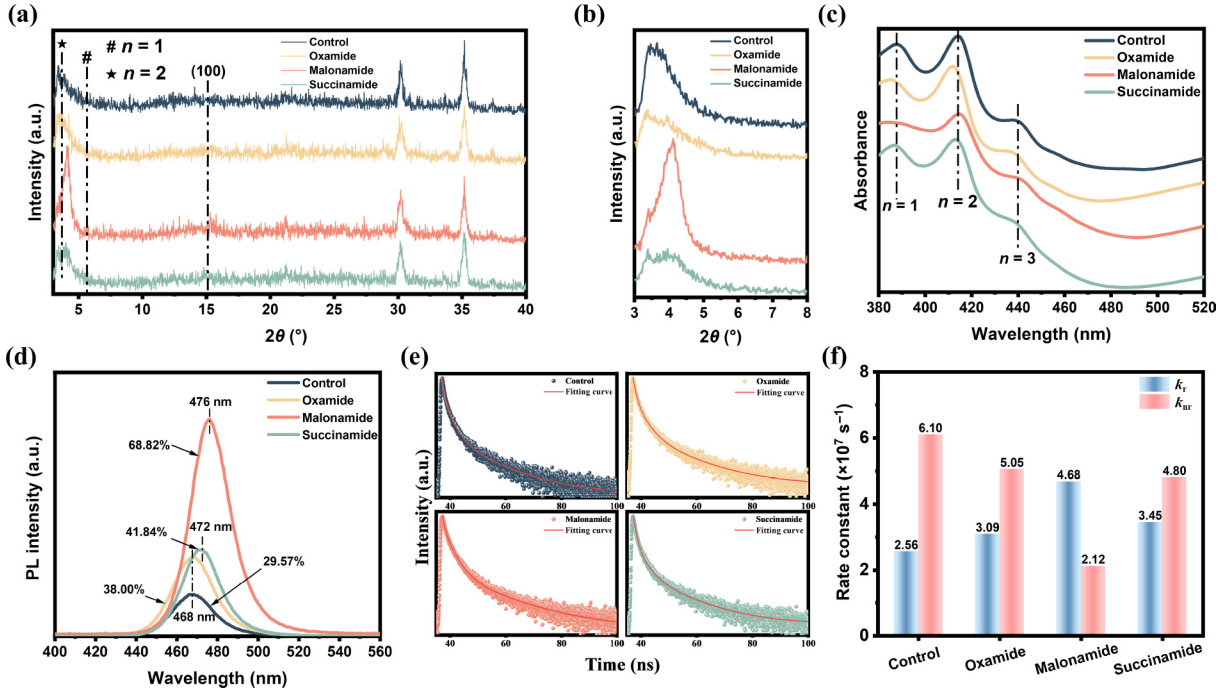

Figure 3 GIXRD patterns (a) with a step of 0.02° at a scanning speed of 4 °·min^{-1} and (b) with a step of 0.02° at a scanning speed of 0.6 °·min^{-1}, (c) UV–vis spectra, (d) PL spectra, (e) TRPL spectra, and (f) calculated recombination rate constants of perovskite.

introduction of different additives, the *n*-phase contribution in the perovskite films was modulated in a controlled manner. The n = 1 phase has been identified as the center for nonradiative recombination losses, which quenches effective exciton and restricts the transfer [30, 31]. Therefore, it is necessary to reduce the n = 1 phase for inhibiting nonradiative recombination. Encouragingly, upon the incorporation of malonamide additive, the relative proportion of the n = 1 phase experiences a substantial decrease and becomes almost negligible, indicating the promising application of malonamide-modified perovskite in PeLED.

The PL spectra (Fig. 3(d)) indicate that the film exhibits the strongest fluorescence intensity for malonamide-modified perovskite. In contrast, the perovskite films modified with oxamide and succinamide display weaker intensities. Furthermore, the perovskite films incorporating malonamide exhibit excellent stability, with minimal degradation in intensity after being exposed to air humidity for 100 min (Fig. S6 in the ESM). The PL intensity evolution aligns with the PLQY results. Control sample exhibits the smallest PLQY (29.57%), and oxamide-, malonamide-, and succinimide-modified samples demonstrate 38.00%, 68.82%, and 41.84%, PLQY, respectively (Fig. 3(d) and Fig. S7 in the ESM). This improvement is likely attributed to passivation and reduction of trap-assisted nonradiative losses. The TRPL decay curves (Fig. 3(e)) were modeled using a triexponential decay function. The physical interpretation of these decay components suggests that the fast decay (τ_1) is associated with nonradiative recombination processes stemming from crystal defects, whereas the slow decay (τ_2 and τ_3) components are attributed to radiative recombination events. As demonstrated in Table S2 in the ESM, the control film exhibits an average decay lifetime (τ_{avg}) of 11.55 ns. Subsequent to additives treatment, the τ_{avg} values of the perovskite films based on oxamide, malonamide, and succinamide increase to 12.28, 14.72, and 12.12 ns, respectively. Additionally, we calculated the rate constants for radiative (k_r) and nonradiative (k_{nr}) recombination in perovskite films, with a focus on control and additives-treated films. These values were obtained through the application of relevant formulas: $\tau_{avg} = 1/(k_r+k_{nr})$ and PLQY = $k_r/(k_r+k_{nr})$, in which k_r and k_{nr} represent the radiative and nonradiative recombination rate constants, respectively. The calculated k_r and k_{nr} were summarized in Fig. 3(f) and Table S3 in the ESM. These fitting calculation results corroborate each other, indicating that the perovskite films treated with malonamide additives exhibit exceptional stability, resulting in a reduction of nonradiative recombination losses and an improvement in radiative recombination efficiency.

For the control films, the integration with the perovskite crystals occurs through PEA^+/BA^+. When malonamide was introduced into the precursor solution, hydrogen bonds originated from amide and ammonium ($-H_2N\cdots H-NH_2^+-$) retarded the diffusion of PEA^+/BA^+, which restricted the nucleation rates of perovskite and the formation of n = 1 phase. At crystallization process, hydrogen bonding between amide and $Pb(Br/Cl)_6^{4-}$ octahedra performed stronger binding force, together with PEA^+/BA^+ that were originally bound to the perovskite crystals. It should be noted that malonamide molecule possesses two separate C=O and $-NH_2$. We deduce that C=O and another $-NH_2$ groups in malonamide bind to the uncoordinated Pb^{2+} and Br^-/Cl^- in perovskite at appropriate angles and bond length, respectively, thereby passivating the defects within the perovskite crystals. Furthermore, we evaluated the distance between two hydrogen ions in two $-NH_2$ groups situated at two sides of malonamide, which extended from 5.7 Å at free status to 7.2 Å at stretched condition. In consideration of intrinsic nature of hydrogen bond, the bond length is usually within 2.0 and 2.9 Å. Theoretically, two halide ions in adjacent $Pb(Br/Cl)_6^{4-}$ octahedron are at distances of 5.8, 9.2, and 11.6 Å, if the bond length of $Pb-Br^-/Cl^-$ in $Pb(Br/Cl)_6^{4-}$ is determined as around 2.9 Å (JCPDS no. 18-0364). Ideally, the duty regions of hydrogen bonds at two sides of malonamide match well with the distance of halide ions in adjacent $Pb(Br/Cl)_6^{4-}$ octahedra, which providing

interactions with a high possibility. Accordingly, two hydrogen bonds, N–H···Br^-/Cl^-, formed between malonamide and perovskite, together with the interaction of C=O and uncoordinated Pb^{2+}, retarded the crystallization process with anchoring halide ions, and passivated the defects. Based on the exceptional performance of the perovskite films, we schematically illustrate the fundamental mechanisms of crystallization kinetics modulated by malonamide (Fig. 4). The negligible modulation effect of other amide, oxamide and succinamide, is originated from the difference in molecular structure. For oxamide, limited molecular chain length restricts its interaction regions and defect sites. For succinamide, required by multifunctional groups work simultaneously, the U-fold of succinamide is optimal in accessing desired defect sites, which is prohibited by its chain rigidity. Even if succinamide is U-folded as expected, it may not persist in the long term.

3.3 Defect passivation

Additionally, for investigating the trap density of perovskite films, we employed the SCLC method and fabricated hole-only devices with the structure of ITO/PEDOT:PSS/LiF/perovskite/MoO_3/Ag. The values of trap-filled limited voltage (V_{TFL}) serve as a pivotal parameter for assessing the density and concentration of defects within perovskite films. Through the SCLC measurement, it can be observed that the V_{TFL} of perovskite films with additives is lower than that of the control perovskite films (Fig. S6 in the ESM). Furthermore, we calculated the trap density of states (N_t) using the formula of $V_{TFL} = eN_tL^2/2\varepsilon_0\varepsilon_r$, and observed a decrease from 4.65 × 10^{17} cm^{-3} (control) to 4.50 × 10^{17} cm^{-3} (oxamide), 3.46 × 10^{17} cm^{-3} (malonamide), and 4.02 × 10^{17} cm^{-3} (succinamide). We calculated the Urbach energy (E_u), which is utilized as a metric to evaluate the defects introduced by localized states within the bandgap. As depicted in Fig. S7 in the ESM, the E_u of the perovskite films modified with amide decreases from 10.24 meV (control) to 9.74 meV (oxamide), 5.47 meV (malonamide), and 10.07 meV (succinamide). Notably, the E_u of perovskite films modified with malonamide exhibits a significant decrease compared to other amides, indicating a high crystallinity of the films and a reduction in defect density.

We conducted an analysis of the trend in variations pertaining to the exciton binding energy (E_b), derived from temperature-dependent PL spectroscopy data. The E_b values for the control and malonamide-treated perovskite films were calculated to be 135.67 and 266.47 meV (Fig. S8 in the ESM), respectively, using the equation $I(T) = I_0/(1+A\exp(-E_b/k_BT))$. An exciton is an electrically neutral quasi-particle consisting of an electron-hole pair bound by Coulombic force, with perovskite films possessing high E_b that is particularly advantageous for luminescent applications [54]. The enhancement of E_b exerts an influence on the concentration of free carriers in perovskites, reducing the likelihood of exciton dissociation into free carriers and enhancing radiative recombination through excitons, which indicates a decrease in nonradiative recombination. Our experimental results demonstrate that perovskite films with additives do exhibit high E_b, suggesting that the incorporation of additives is an effective strategy for suppressing nonradiative recombination.

3.4 Carrier transfer dynamics

The photogenerated carrier recombination and transfer dynamics of control and malonamide-treated perovskite films on the picosecond (ps) timescale were investigated using TAS. As shown in Figs. 5(a) and 5(b), for both quasi-2D perovskite films, three ground-state bleach (GSB) signals were observed at approximately 417, 446, and 462 nm, assigned to the n = 2, 3, and ≥ 4 phases, respectively. Within 0.1 ps, the pump light rapidly accumulated at the n = 2 and 3 GSB peaks, indicating that at the initial stage, photogenerated carriers were primarily excited in the small-n phases (n = 2 and 3). Due to the quantum confinement effect, in quasi-2D perovskite structures, larger n values correspond to smaller bandgaps. Therefore, when multiple phases coexist, energy transfer can be anticipated, which is confirmed by the TA signals. As shown in Figs. 5(c) and 5(d), the evolution of the TA spectra from 0 to 5 ps clearly demonstrates the migration of carriers from the small-n phases to the large-n phases [55, 56]. Within a relatively short decay time, the signals associated with the small-n phases (n = 2 and 3) decreased, while the peak intensities in the large-n phases (n ≥ 4) gradually increased. This carrier transfer from phases with larger bandgaps to those with smaller bandgaps indicates an efficient energy transfer process from the small-n phases to the large-

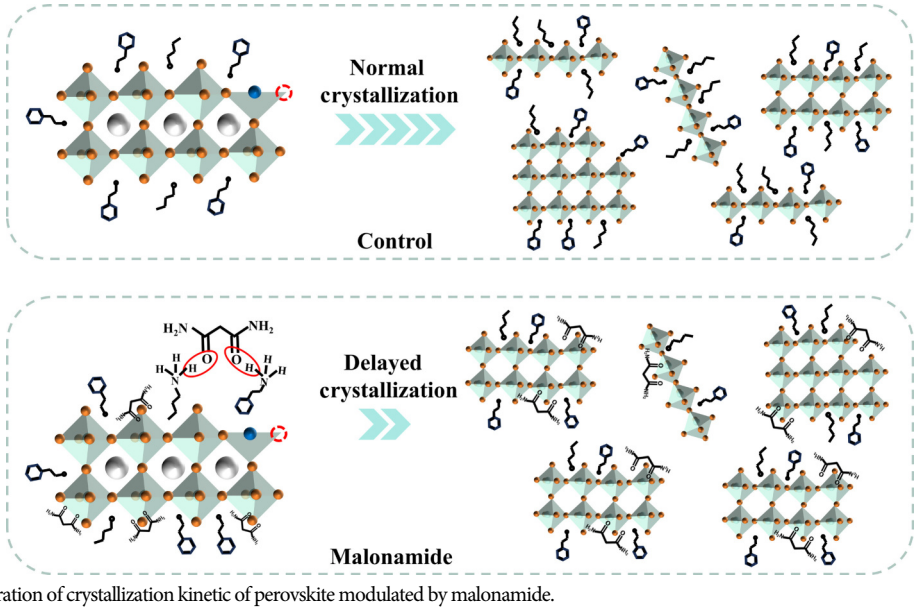

Figure 4 Schematic illustration of crystallization kinetic of perovskite modulated by malonamide.

n phases. The intensity evolution of the GSB peaks corresponds to the evolution of the excited-state population in the respective phases [57]. Here, the variation of GSB intensities within 5 ps illustrates the relative exciton contributions (Figs. 5(e) and 5(f)). Notably, at 0.5 ps, the extracted phase distribution for the control film is dominated by the n = 3 phase (Fig. 5(e)), whereas the phase distribution for the perovskite film with the malonamide additive is dominated by the $n \geq 4$ phase (Fig. 5(f)). This suggests that the carriers transfer from the n = 2 phase to the $n \geq 4$ phase occurs more rapidly and efficiently in malonamide-treated perovskite film. These results indicate that the addition of malonamide optimizes the phase distribution and facilitates efficient and rapid energy transfer to the large-*n* phase in 2D perovskite.

3.5 Device performance

We introduced malonamide into quasi-2D perovskite precursor solution as an additive to verify the advantages and fabricated PeLED to evaluate the performance of the device with structure of ITO/PEDOT:PSS/LiF/perovskite/TPBi/LiF/Al (Fig. 6(a)). The optimal concentration of malonamide (5 mg/500 μL) is selected for

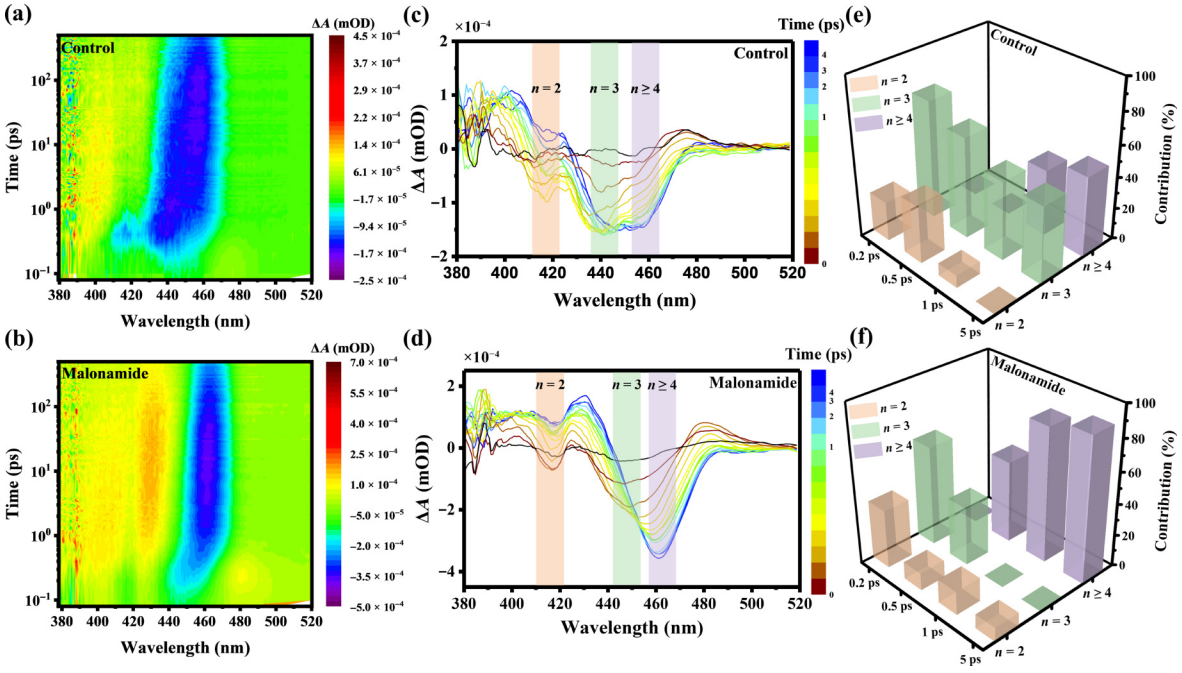

Figure 5 TA time spectrograms of (a) control and (b) malonamide-modified perovskite films. TA spectra at different probe delay times of (c) control and (d) malonamide-modified perovskite films. The exciton contributions derived from different phases of (e) control and (f) malonamide-modified perovskite films, based on the intensity measurements of GSB in TA spectra.

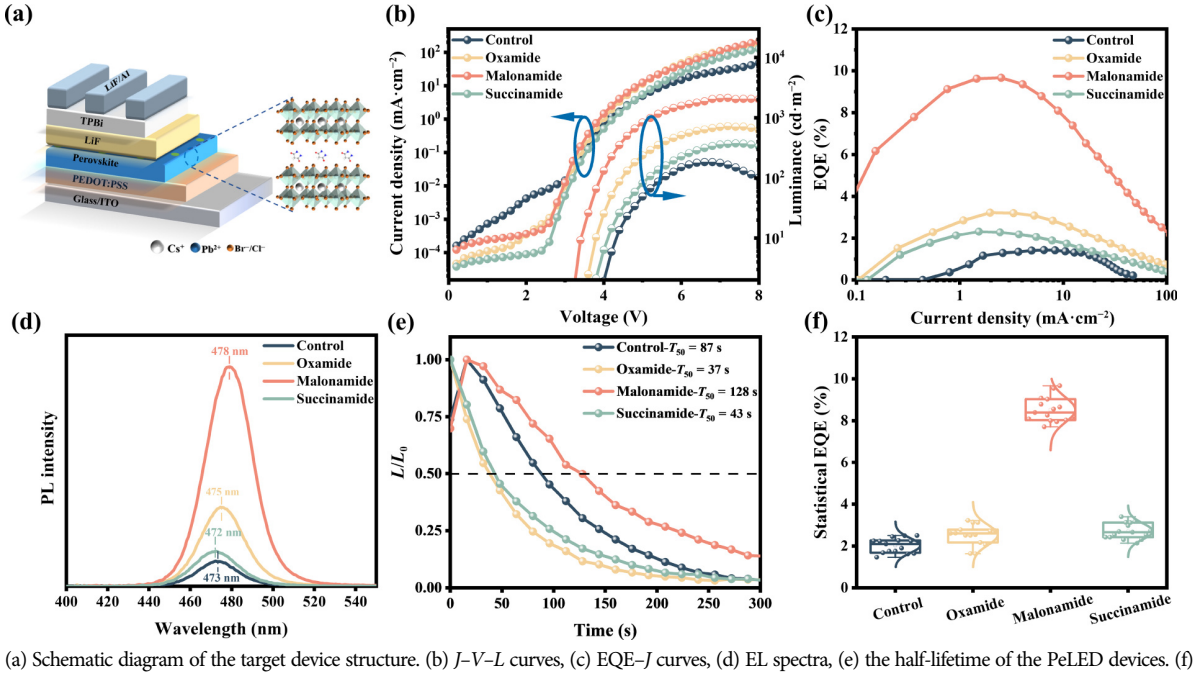

Figure 6 (a) Schematic diagram of the target device structure. (b) *J*–*V*–*L* curves, (c) EQE–*J* curves, (d) EL spectra, (e) the half-lifetime of the PeLED devices. (f) EQE_{max} histogram of PeLED measured from 15 devices.

subsequent device fabrication (Fig. S11 in the ESM). The *J*–*V*–*L* characteristics of the typical devices are shown in Fig. 6(b). The improvement of the current efficiency in the amide-modified devices is due to the leakage current arising from the reduction of the trap defects. Particularly, the device inserted with malonamide exhibited the highest EQE (9.7%) and brightest luminance (2063 $cd \cdot m^{-2}$) at a wavelength of 478 nm (Fig. 6(c)), which partially originated from the reduction of nonradiative recombination loss due to the passivation of perovskite defects and the optimized *n*-phase distribution. Additionally, EL spectra indicate a red shift to 478 nm for the malonamide-treated devices (Fig. 6(d)), which is consistent with the PL results in Fig. 3(d). We demonstrated the performance data of amide-modified devices in Table S4 in the ESM. We characterized the stability of PeLED, as shown in Fig. 6(e): The half-lifetime (T_{50}) of the PeLED increases from 87 s for the control device to 128 s for the malonamide-additive device. The EL spectra under increasing voltages and a constant current density are shown in Figs. S12 and S13 in the ESM, which demonstrated the enhanced color stability of malonamide based PeLED. The reproducibility of devices performance is demonstrated by the box plot in Fig. 6(f), which presents EQE data for 15 devices. To highlight the role of malonamide as an additive, we fabricated a device with malonamide as the buried interface (Device structure: ITO/PEDOT:PSS/Malonamide/perovskite/TPBi/LiF/Al, as depicted in Fig. S14 in the ESM). The experiment results show that the performance of the device made by adding malonamide to perovskite is significantly better than that with the malonamide buried modification. (Fig. S15 and Table S5 in the ESM).

4 Conclusion

In this work, we propose amide as additives to modulate crystallization kinetics of perovskite films. Among them, malonamide exhibits the most effective roles. The functional groups of malonamide act as Lewis acids/bases, binding to uncoordinated lead ions in adjacent perovskite crystals at appropriate angles and bond lengths, while simultaneously forming hydrogen bonds with halogen ions. The incorporation of malonamide additives enhances the PLQY and TRPL of perovskite films. The hydrogen bonds induce the redistribution of *n*-phase and reduce the formation of *n* = 1 phase, thereby suppressing nonradiative recombination and elevating the carrier transport, which enables rapid and efficient energy transfer across various phases. High-performance pure-blue PeLED incorporating malonamide were achieved with EQE of 9.7% at 478 nm.

Electronic Supplementary Material: Supplementary material (*in-situ* PL measurements, PLQY, SCLC, temperature-dependent PL measurements, Urbach energy and device characteristics) is available in the online version of this article at https://doi.org/10.26599/NR.2025.94907920.

Data availability

All data needed to support the conclusions in the paper are presented in the manuscript and the Electronic Supplementary Material. Additional data related to this paper may be requested from the corresponding author upon request.

Acknowledgements

The authors are grateful for the support from the Key R&D Program of Zhejiang Province (No. 2024C01193), the National Natural Science Foundation of China (Nos. 52171145 and 52102293), and the Graduate Scientific Research Foundation of Wenzhou University.

Declaration of competing interest

All the contributing authors report no conflict of interests in this work.

Author contribution statement

Z. Y. G.: Writing – original raft, formal analysis, data curation. R. Y. L.: Investigation, methodology, validation. B. Z.: Data curation, investigation, validation. M. H. L.: Conceptualization, data curation, software. Z. J. L.: Formal analysis, visualization. L. L. Z.: Formal analysis, methodology. Q. M.: Resources, visualization. H. H.: Conceptualization, funding acquisition, supervision. Y. Y.: Writing – review & editing, resources. H. H. W.: Resources, software. G. K. C.: Investigation, project administration, supervision. J. Z.: Project administration, supervision. C. Z.: Writing – review & editing, supervision, funding acquisition.

Use of AI statement

None.

References

[1] Zhang, J. F.; Wang, L.; Zhang, X. Y.; Xie, G. H.; Jia, G. H.; Zhang, J. H.; Yang, X. Y. Blue light-emitting diodes based on halide perovskites: Recent advances and strategies. *Mater. Today* **2021**, *51*, 222–246.

[2] Sun, Y. Q.; Ge, L. S.; Dai, L. J.; Cho, C.; Ferrer Orri, J.; Ji, K. Y.; Zelewski, S. J.; Liu, Y.; Mirabelli, A. J.; Zhang, Y. C. et al. Bright and stable perovskite light-emitting diodes in the near-infrared range. *Nature* **2023**, *615*, 830–835.

[3] Li, G. P.; Huang, J. S.; Li, Y. Q.; Tang, J. X.; Jiang, Y. Highly bright and low turn-on voltage $CsPbBr_3$ quantum dot LEDs via conjugation molecular ligand exchange. *Nano Res.* **2019**, *12*, 109–114.

[4] Liu, X. K.; Xu, W. D.; Bai, S.; Jin, Y. Z.; Wang, J. P.; Friend, R. H.; Gao, F. Metal halide perovskites for light-emitting diodes. *Nat. Mater.* **2021**, *20*, 10–21.

[5] Wang, Y. Y.; Xu, Y. T.; Yun, J. Y.; Cai, Q. T.; Zhai, L. L.; Zhuang, D. C.; Yang, G. H.; Huang, H.; Li, M. H.; Yang, Y. et al. Suppressing interfacial nonradiative recombination by alkali hydroxides for efficient blue perovskite light-emitting diodes. *Chem. Eng. J.* **2024**, *486*, 149964.

[6] Tan, Z. K.; Moghaddam, R. S.; Lai, M. L.; Docampo, P.; Higler, R.; Deschler, F.; Price, M.; Sadhanala, A.; Pazos, L. M.; Credgington, D. et al. Bright light-emitting diodes based on organometal halide perovskite. *Nat. Nanotechnol.* **2014**, *9*, 687–692.

[7] Kong, L. M.; Sun, Y. Q.; Zhao, B.; Ji, K. Y.; Feng, J.; Dong, J. C.; Wang, Y. Z.; Liu, Z. R.; Maqbool, S.; Li, Y. G. et al. Fabrication of red-emitting perovskite LEDs by stabilizing their octahedral structure. *Nature* **2024**, *631*, 73–79.

[8] Liu, Z.; Qiu, W. D.; Peng, X. M.; Sun, G. W.; Liu, X. Y.; Liu, D. H.; Li, Z. C.; He, F. R.; Shen, C. Y.; Gu, Q. et al. Perovskite light-emitting diodes with EQE exceeding 28% through a synergetic dual-additive strategy for defect passivation and nanostructure regulation. *Adv. Mater.* **2021**, *33*, 2103268.

[9] Chen, F.; Ming, W. J.; Li, Y. F.; Gao, Y.; Pasquale, L.; Yao, K. X.; Huang, B. Y.; Cai, Q. T.; Lu, G. C.; Song, J. Z. et al. Highly spectra-stable pure blue perovskite light-emitting diodes based on copper and potassium co-doped quantum dots. *Nano Res.* **2023**, *16*, 7654–7660.

[10] Kojima, A.; Teshima, K.; Shirai, Y.; Miyasaka, T. Organometal halide perovskites as visible-light sensitizers for photovoltaic cells. *J. Am. Chem. Soc.* **2009**, *131*, 6050–6051.

[11] Gao, Y.; Cai, Q. T.; He, Y. F.; Zhang, D. S.; Cao, Q. L.; Zhu, M. Y.; Ma, Z. C.; Zhao, B. D.; He, H. P.; Di, D. W. et al. Highly efficient blue light-emitting diodes based on mixed-halide perovskites with reduced chlorine defects. *Sci. Adv.* **2024**, *10*, eado5645.

[12] Xia, Y.; Li, Y. H.; Wang, Z. K.; Liao, L. S. Domain distribution management of quasi-2D perovskites toward high-performance blue light-emitting diodes. *Adv. Funct. Mater.* **2023**, *33*, 2303423.

[13] Zhang, K.; Shen, Y.; Cao, L. X.; Su, Z. H.; Hu, X. M.; Feng, S. C.; Wang, B. F.; Xie, F. M.; Li, H. Z.; Gao, X. Y. et al. Nondestructive halide exchange via S_N2-like mechanism for efficient blue perovskite light-emitting diodes. *Nat. Commun.* **2024**, *15*, 10621.

[14] Jia, Y. H.; Li, R. C.; Zhou, Y.; Zhao, S. H.; Yu, H.; Wang, J. P.; Lin, Z. Y.; Su, H. B.; Zhao, N. Unveiling the complex evolution in mixed Br-Cl perovskite precursors for high-efficiency deep-blue light-emitting diodes. *Small Struct.* **2023**, *4*, 2200393.

[15] Zeng, M. X.; Chen, D.; Wang, J. J.; Li, D. Y.; Xie, G. Y.; Ou, J. Q.; Wang, L.; Wang, J. Deep-blue perovskite light-emitting diodes realized by a dynamic interfacial ion exchange. *ACS Appl. Mater. Interfaces* **2023**, *15*, 36620–36627.

[16] Wang, S. X.; Yu, Z. Q.; Yang, X. F.; Chen, G. Y.; Dong, C. M.; Fu, H. H.; Ke, W. J.; Fang, G. J. Multifunctional additives with cation-π interactions enable high-performance blue perovskite light-emitting diodes. *ACS Energy Lett.* **2025**, *10*, 1183–1191.

[17] Zhou, Y. H.; Lou, Y. H.; Wang, X. Q.; Wang, K. L.; Chen, J.; Chen, C. H.; Wang, Z. K. Spectral stable blue perovskite light-emitting diodes by introducing organometallic ligand. *Adv. Opt. Mater.* **2022**, *10*, 2101655.

[18] Xia, Y.; Lou, Y. H.; Zhou, Y. H.; Shi, Y. R.; Wang, K. L.; Cai, L.; Chen, C. H.; Hu, F.; Wang, Z. K.; Liao, L. S. Reduced confinement effect by isocyanate passivation for efficient sky-blue perovskite light-emitting diodes. *Adv. Funct. Mater.* **2022**, *32*, 2208538.

[19] Dong, J. C.; Zhao, B.; Ji, H. Y.; Zang, Z. A.; Kong, L. M.; Chu, C. S.; Han, D. Y.; Wang, J.; Fu, Y. H.; Zhang, Z. H. et al. Multivalent-effect immobilization of reduced-dimensional perovskites for efficient and spectrally stable deep-blue light-emitting diodes. *Nat. Nanotechnol.* **2025**, *20*, 507–514.

[20] Ko, P. K.; Ge, J. C.; Ding, P. B.; Chen, D. Z.; Tsang, H. L. T.; Kumar, N.; Halpert, J. E. The deepest blue: Major advances and challenges in deep blue emitting quasi-2D and nanocrystalline perovskite LEDs. *Adv. Mater.* **2025**, *37*, 2407764.

[21] Kong, L. M.; Zhang, X. Y.; Li, Y. G.; Wang, H. R.; Jiang, Y. Z.; Wang, S.; You, M. Q.; Zhang, C. X.; Zhang, T.; Kershaw, S. V. et al. Smoothing the energy transfer pathway in quasi-2D perovskite films using methanesulfonate leads to highly efficient light-emitting devices. *Nat. Commun.* **2021**, *12*, 1246.

[22] Yang, C. Y.; Wan, Y. F.; Xu, X. J.; Zhang, H.; Liu, Y. G.; Tong, J. F.; Li, J. F.; Wang, K. L. Synergistic crystallization regulation and defect passivation via dual additives for high-efficiency quasi-2D perovskite light-emitting diodes. *ACS Appl. Electron. Mater.* **2025**, *7*, 3686–3693.

[23] Fang, Z. B.; Chen, W. J.; Shi, Y. L.; Zhao, J.; Chu, S. L.; Zhang, J.; Xiao, Z. G. Dual passivation of perovskite defects for light-emitting diodes with external quantum efficiency exceeding 20%. *Adv. Funct. Mater.* **2020**, *30*, 1909754.

[24] Zhuang, D. C.; Wang, Y. Y.; Cai, Q. T.; Zhai, L. L.; Huang, H.; Yang, G. H.; Yang, Y.; Zhang, L. J.; Zou, C. Restraint of nonradiative recombination via modulation of *n*-phase distribution through interfacial lithium salt insertion for high-performance pure-blue perovskite LEDs. *ACS Appl. Mater. Interfaces* **2024**, *16*, 31274–31282.

[25] Kim, D. H.; Muzzillo, C. P.; Tong, J. H.; Palmstrom, A. F.; Larson, B. W.; Choi, C.; Harvey, S. P.; Glynn, S.; Whitaker, J. B.; Zhang, F. et al. Bimolecular additives improve wide-band-gap perovskites for efficient tandem solar cells with CIGS. *Joule* **2019**, *3*, 1734–1745.

[26] Liu, Y. J.; Wang, S. X.; Yu, Z. Q.; Chen, G. Y.; Wang, C.; Wang, T.; Ke, W. J.; Fang, G. J. A multifunctional additive strategy enables efficient pure-blue perovskite light-emitting diodes. *Adv. Mater.* **2023**, *35*, 2302161.

[27] Wang, B.; Lou, Y. H.; Xia, Y.; Hu, F.; Li, Y. H.; Wang, K. L.; Chen, J.; Chen, C. H.; Su, Z. H.; Gao, X. Y. et al. Chemical reaction modulated low-dimensional phase toward highly efficient sky-blue perovskite light-emitting diodes. *Angew. Chem., Int. Ed.* **2024**, *63*, e202406140.

[28] Wang, H. Y.; Zou, W. J.; Luo, H.; Quan, Y. H.; Yang, L.; Liu, X. C.; Li, H. M. Ion migration inhibition and defect passivation via sulfonate salt coordination for high-performance perovskite solar cells with enhanced phase stability. *J. Mater. Chem. C* **2023**, *11*, 13518–13525.

[29] Zhang, F. J.; Song, J. Z.; Cai, B.; Chen, X.; Wei, C. T.; Fang, T.; Zeng, H. B. Stabilizing electroluminescence color of blue perovskite LEDs via amine group doping. *Sci. Bull.* **2021**, *66*, 2189–2198.

[30] Yang, X. Y.; Ma, L.; Yu, M. T.; Chen, H. H.; Ji, Y. Q.; Hu, A.; Zhong, Q. X.; Jia, X. H.; Wang, Y. J.; Zhang, Y. Z. et al. Focus on perovskite emitters in blue light-emitting diodes. *Light: Sci. Appl.* **2023**, *12*, 177.

[31] Yuan, S.; Wang, Z. K.; Xiao, L. X.; Zhang, C. F.; Yang, S. Y.; Chen, B. B.; Ge, H. T.; Tian, Q. S.; Jin, Y.; Liao, L. S. Optimization of low-dimensional components of quasi-2D perovskite films for deep-blue light-emitting diodes. *Adv. Mater.* **2019**, *31*, 1904319.

[32] Zhao, B. D.; Lian, Y. X.; Cui, L. S.; Divitini, G.; Kusch, G.; Ruggeri, E.; Auras, F.; Li, W. W.; Yang, D. X.; Zhu, B. N. et al. Efficient light-emitting diodes from mixed-dimensional perovskites on a fluoride interface. *Nat. Electron.* **2020**, *3*, 704–710.

[33] Jiang, M. W.; Zhang, X. M.; Wang, F. J. Enabling monodisperse perovskite phase with buried interface modification toward efficient light-emitting diodes. *Nano Res. Energy* **2023**, *2*, e9120069.

[34] Neese, F. Software update: The ORCA program system-Version 5.0. *WIREs Comput. Mol. Sci.* **2022**, *12*, e1606.

[35] Kossmann, S.; Neese, F. Comparison of two efficient approximate Hartee-Fock approaches. *Chem. Phys. Lett.* **2009**, *481*, 240–243.

[36] Stephens, P. J.; Devlin, F. J.; Chabalowski, C. F.; Frisch, M. J. *Ab initio* calculation of vibrational absorption and circular dichroism spectra using density functional force fields. *J. Phys. Chem.* **1994**, *98*, 11623–11627.

[37] Weigend, F.; Ahlrichs, R. Balanced basis sets of split valence, triple zeta valence and quadruple zeta valence quality for H to Rn: Design and assessment of accuracy. *Phys. Chem. Chem. Phys.* **2005**, *7*, 3297–3305.

[38] Caldeweyher, E.; Bannwarth, C.; Grimme, S. Extension of the D3 dispersion coefficient model. *J. Chem. Phys.* **2017**, *147*, 034112.

[39] Caldeweyher, E.; Ehlert, S.; Hansen, A.; Neugebauer, H.; Spicher, S.; Bannwarth, C.; Grimme, S. A generally applicable atomic-charge dependent London dispersion correction. *J. Chem. Phys.* **2019**, *150*, 154122.

[40] Zheng, J. J.; Xu, X. F.; Truhlar, D. G. Minimally augmented Karlsruhe basis sets. *Theor. Chem. Acc.* **2011**, *128*, 295–305.

[41] Lu, T.; Chen, F. W. Multiwfn: A multifunctional wavefunction analyzer. *J. Comput. Chem.* **2012**, *33*, 580–592.

[42] Lu, T. A comprehensive electron wavefunction analysis toolbox for chemists, Multiwfn. *J. Chem. Phys.* **2024**, *161*, 082503.

[43] Lu, T.; Chen, F. W. Quantitative analysis of molecular surface based on improved Marching Tetrahedra algorithm. *J. Mol. Graphics Modell.* **2012**, *38*, 314–323.

[44] Humphrey, W.; Dalke, A.; Schulten, K. VMD: Visual molecular dynamics. *J. Mol.Graphics* **1996**, *14*, 33–38.

[45] Cheng, L. P.; Huang, J. S.; Shen, Y.; Li, G. P.; Liu, X. K.; Li, W.; Wang, Y. H.; Li, Y. Q.; Jiang, Y.; Gao, F. et al. Efficient $CsPbBr_3$ perovskite light-emitting diodes enabled by synergetic morphology control. *Adv. Opt. Mater.* **2019**, *7*, 1801534.

[46] Min, H.; Chang, J.; Tong, Y. F.; Wang, J. Q.; Zhang, F.; Feng, Z. Q.; Bi, X. Y.; Chen, N. N.; Kuang, Z. Y.; Wang, S. X. et al. Additive treatment yields high-performance lead-free perovskite light-emitting diodes. *Nat. Photonics* **2023**, *17*, 755–760.

[47] Liu, Z. R.; Wang, G. L.; Kong, L. M.; Wang, J. H.; Wang, Y. Z.; Du, P.; Wang, L.; Wang, S.; Rogach, A. L.; Yang, X. Y. Simultaneous regulation of crystallization and suppression of oxidation in $CsSnI_3$ perovskite enables efficient and stable near-infrared light-emitting diodes. *Nano Lett.* **2025**, *25*, 7061–7068.

[48] Ma, J. J.; Qin, M. C.; Li, P. W.; Han, L. Y.; Zhang, Y. Q.; Song, Y. L. Crystallization kinetics modulation and defect suppression of all-inorganic $CsPbX_3$ perovskite films. *Energy Environ. Sci.* **2022**, *15*, 413–438.

[49] Bai, W. H.; Liang, M. M.; Xuan, T. T.; Gong, T.; Bian, L.; Li, H. L.; Xie, R. J. Ligand engineering enables efficient pure red tin-based perovskite light-emitting diodes. *Angew. Chem., Int. Ed.* **2023**, *62*, e202312728.

[50] Gao, W. H.; Ding, J. K.; Ma, Q. X.; Zhang, H.; Zhang, J. J.; Zhang, Z. L.; Li, M. J.; Wang, Y.; Zhang, B. X.; Pauporté, T. et al. Synergistic modulation of orientation and steric hindrance induced by alkyl chain length in ammonium salt passivator toward high-performance inverted perovskite solar cells and modules. *Adv. Mater.* **2025**, *37*, 2413304.

[51] Jiang, M. W.; Zhang, X. M.; Wang, F. J. Efficient perovskite nanograin light-emitting diodes in green-to-blue gamut with co-additive engineering. *Adv. Mater.* **2024**, *36*, 2400565.

[52] Jiang, M. W.; Li, L.; Qi, Z. W.; Wang, F. J. Efficient Rec. 2020 compliant pure-green mixed-cation perovskite light-emitting diodes with multifunctional co-additives. *Adv. Mater.* **2025**, *37*, 2503683.

[53] Bao, Z. Q.; Yu, S. L.; Guo, X. Y.; Wang, Y. P.; Lv, Y.; Zou, D. Y.; Song, L.; Liu, X. Y. Regulating the continuous and concentrated distribution of Quasi-2D perovskite phases to achieve Sky-Blue Light-Emitting diodes with efficiency approaching 17%. *Chem. Eng. J.* **2024**, *482*, 148875.

[54] Jiang, Y.; Wang, X.; Pan, A. L. Properties of excitons and photogenerated charge carriers in metal halide perovskites. *Adv. Mater.* **2019**, *31*, 1806671.

[55] Shang, Q. Y.; Wang, Y. N.; Zhong, Y. G.; Mi, Y.; Qin, L.; Zhao, Y. F.; Qiu, X. H.; Liu, X. F.; Zhang, Q. Unveiling structurally engineered carrier dynamics in hybrid quasi-two-dimensional perovskite thin films toward controllable emission. *J. Phys. Chem. Lett.* **2017**, *8*, 4431–4438.

[56] Wang, N. N.; Cheng, L.; Ge, R.; Zhang, S. T.; Miao, Y. F.; Zou, W.; Yi, C.; Sun, Y.; Cao, Y.; Yang, R. et al. Perovskite light-emitting diodes based on solution-processed self-organized multiple quantum wells. *Nat. Photonics* **2016**, *10*, 699–704.

[57] Quan, L. N.; Zhao, Y. B.; García de Arquer, F. P.; Sabatini, R.; Walters, G.; Voznyy, O.; Comin, R.; Li, Y. Y.; Fan, J. Z.; Tan, H. R. et al. Tailoring the energy landscape in quasi-2D halide perovskites enables efficient green-light emission. *Nano Lett.* **2017**, *17*, 3701–3709.